Model predictions and comparisons for three toxicokinetic models for the systemic transport of trichloroethylene

H.T. Banks* and Laura K. Potter†
Center for Research in Scientific Computation
North Carolina State University
Raleigh, NC 27695-8205

September 6, 2001

Abstract

In this paper we present and compare three physiologically based pharmacokinetic models for the systemic transport of trichloroethylene (TCE), a common environmental toxicant. Of particular interest is the disposition of TCE in the adipose tissue, where TCE is known to accumulate. The first two systemic models utilize standard ODE-based adipose compartments that assume rapid equilibrium and uniformity. The third model includes a PDE-based axial dispersion model that is designed to capture the heterogeneous physiology of adipose tissue and the expected transport of TCE there.

Using numerical methods and model simulations, we compare the predicted concentration profiles of TCE in the adipose tissue for the three systemic models. Our results suggest that the dispersion-based adipose compartmental model is best able to capture the physiological heterogeneities of adipose tissue and their expected effects on TCE adipose concentrations.

1 Introduction

Trichloroethylene (TCE) is a solvent that has been used widely in industry as a metal-degreasing agent. This highly lipophilic chemical is now a common soil and groundwater contaminant, and can be found at Superfund sites and Department of Defense facilities across the United States [21]. Numerous studies have linked TCE and several of its metabolites to toxic effects in humans and animals. Acute exposure to TCE is associated with fatigue, headaches, dizziness and drowsiness [12], while chronic exposure has been linked to developmental defects and kidney, liver and lung tumors [6, 7, 8, 13, 15, 20]. TCE is highly soluble in lipids, and is known to accumulate in the adipose (fat) tissue of humans and animals. This important characteristic of TCE has major implications on its dynamics inside the organs and tissues, and on the overall amount of time it takes for TCE to be eliminated from the body.

Physiologically based pharmacokinetic (PBPK) models are used to describe the systemic transport behavior of compounds such as TCE. These compartmental models are useful in determining the effective dosage level received by each of the organs and tissues, and are an important part of the overall process of determining a compound's toxicity in humans and animals. PBPK models usually involve a system of coupled algebraic and differential equations, where each equation represents the transport of the compound through a given organ or tissue. The standard compartmental equations are based on assumptions of rapid equilibrium and uniformity in concentrations within that particular tissue.

These "well-mixed" assumptions may not be appropriate for highly lipophilic chemicals such as TCE inside the adipose tissue, as several studies have demonstrated large degrees of physiological heterogeneities in fat tissue. These heterogeneities include wide variations in fat cell size, metabolic activity, blood flow rates and cell membrane permeabilities [9, 10, 14, 19]. Moreover, it is known that there are varying amounts of

*Author to whom correspondence should be addressed.
†Current address: National Health and Environmental Effects Research Laboratory, U.S. Environmental Protection Agency, Research Triangle Park, NC.

lipid in each fat cell, which leads to an uneven distribution of lipid throughout the adipose tissue [14]. This uneven lipid distribution together with the other heterogeneous properties of adipose tissue strongly suggest that TCE and other lipophilic compounds are likely to have spatially varying concentrations in the adipose tissue. Therefore a spatially varying model may be most appropriate for the transport of TCE within the fat.

To test this hypothesis, we have developed three PBPK models for the systemic transport of TCE, where each model has a different submodel for the adipose tissue compartment [1, 17]. The first two adipose compartmental models are based on the standard "well-mixed" assumptions used in PBPK modeling. The third systemic model is a PBPK-hybrid model with an axial dispersion-based compartmental model for the adipose tissue. This spatially varying submodel is based specifically on the physiology of adipose tissue and the expected transport of TCE within the tissue.

In this paper we present and compare these three PBPK whole-body models for TCE. Using model simulations, we demonstrate that the hybrid model with the spatially varying adipose compartment is most appropriate for this case and is best able to predict the expected transport of TCE inside the adipose tissue.

2 A PBPK model for TCE with a perfusion-limited adipose tissue compartment

First we present a standard PBPK model proposed in [1, 17] which has a perfusion-limited adipose tissue compartment. This model is based on experimental and computational work carried out by Evans et al. [11], who developed a PBPK model for inhaled TCE in Long-Evans rats. The compartments included in the model are: lung, arterial blood, venous blood, brain, kidney, liver, muscle, fat and remaining tissue. See Figure 1 for a geometrical representation of the model.

Each of these compartments except for the lung and blood compartments is modeled as a "perfusion-limited" compartment, in which the blood flow rate to the tissue is assumed to be much *slower* than the rate of diffusion of TCE across cell membranes within that particular tissue [16]. The liver compartment has an additional sink term that represents the metabolism of TCE via Cytochrome P450, which is modeled with Michaelis-Menten kinetics. The lung model is based on a steady-state assumption that leads to an algebraic equation for the concentration of TCE in the arterial blood [16], and the venous blood compartment is modeled as a differential equation that is based on mass balance.

The coupled system of model equations is given by

$$V_f \frac{dC_f}{dt} = Q_f(C_a - \frac{C_f}{P_f}) \tag{1}$$

$$V_v \frac{dC_v}{dt} = Q_m \frac{C_m}{P_m} + Q_t \frac{C_t}{P_t} + Q_f \frac{C_f}{P_f} + Q_{br} \frac{C_{br}}{P_{br}} + Q_l \frac{C_l}{P_l} + Q_k \frac{C_k}{P_k} - Q_c C_v \tag{2}$$

$$C_a = \frac{Q_c C_v + Q_p C_c}{Q_c + \frac{Q_p}{P_b}} \tag{3}$$

$$V_{br} \frac{dC_{br}}{dt} = Q_{br}(C_a - \frac{C_{br}}{P_{br}}) \tag{4}$$

$$V_k \frac{dC_k}{dt} = Q_k(C_a - \frac{C_k}{P_k}) \tag{5}$$

$$V_l \frac{dC_l}{dt} = Q_l(C_a - \frac{C_l}{P_l}) - \frac{v_{max} C_l}{k_M P_l + C_l} \tag{6}$$

$$V_m \frac{dC_m}{dt} = Q_m(C_a - \frac{C_m}{P_m}) \tag{7}$$

$$V_t \frac{dC_t}{dt} = Q_t(C_a - \frac{C_t}{P_t}). \tag{8}$$

The subscripts denote the following specific tissues:

$$f \quad \Leftrightarrow \quad \text{Fat}$$

PBPK Model for Inhaled TCE

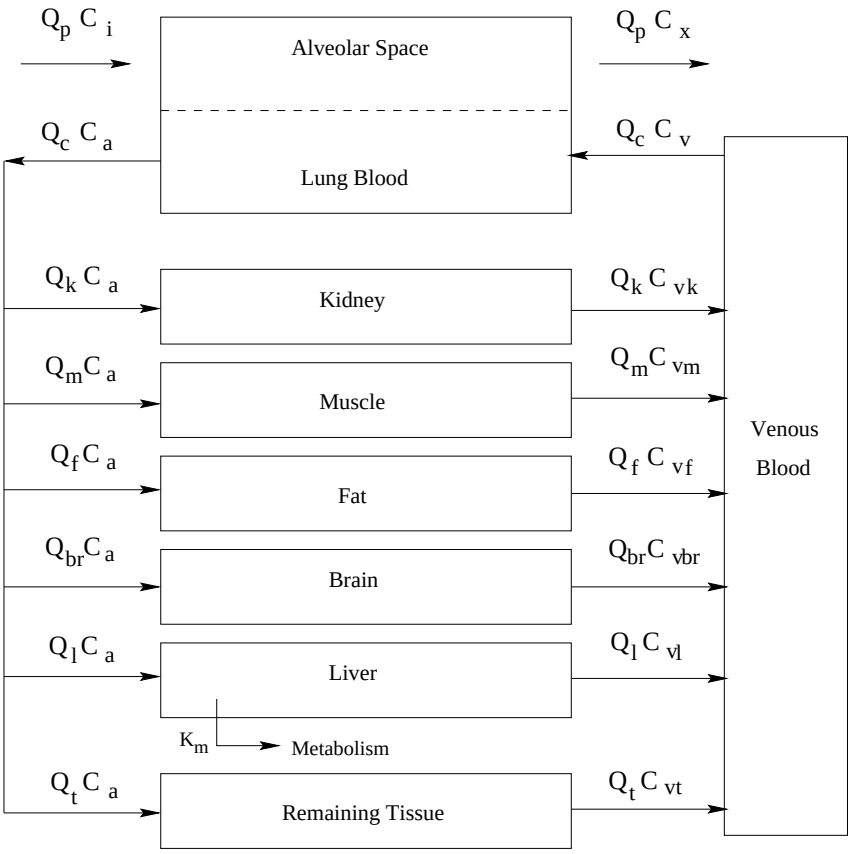

Figure 1: PBPK model for inhaled TCE with a perfusion-limited compartment for adipose tissue. TCE concentrations are denoted by C and blood flow rates are denoted by Q.

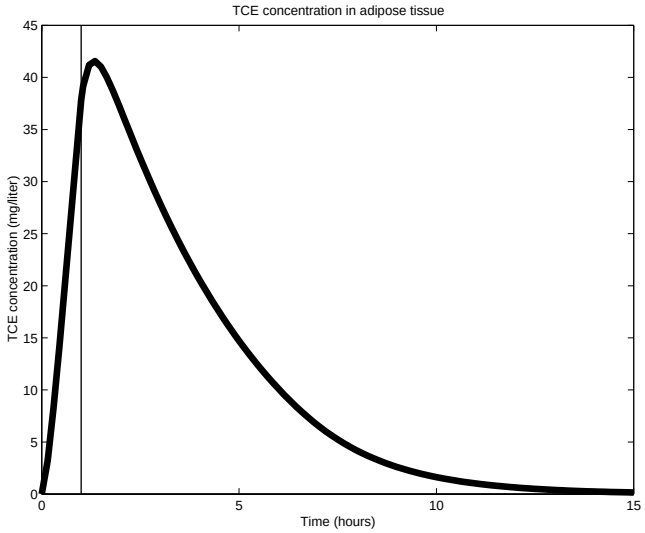

Figure 2: Model simulation: Concentration in time of unbound TCE inside the perfusion-limited fat compartment.

$$
\begin{aligned}
v &\Leftrightarrow \text{Venous blood} \\
a &\Leftrightarrow \text{Arterial blood} \\
br &\Leftrightarrow \text{Brain} \\
k &\Leftrightarrow \text{Kidney} \\
l &\Leftrightarrow \text{Liver} \\
m &\Leftrightarrow \text{Muscle} \\
t &\Leftrightarrow \text{Remaining non-fat tissue.}
\end{aligned}
$$

Total concentrations (in mg/liter) in each of the specific tissues are denoted by C, volumes (in liters) by V, and flow rates (liters/hour) are denoted by Q, each with subscripts corresponding to the specific tissue. The parameters P are the blood/tissue partition coefficients for the respective tissues. See [1, 17] for a complete description of the model equations and parameters. A list of the model parameters is given in the appendix.

Model simulations for (1) – (8) were generated in Matlab using code and model parameters from [11]. For this simulation we chose the forcing function to simulate inhaled TCE as in the experiments carried out by Evans et al. [11]. Specifically, we defined the chamber air concentration $C_c(t)$ to be 2000 parts per million TCE for one hour, followed by fourteen hours of zero TCE concentration.

Figure 2 depicts simulated unbound TCE concentrations in the perfusion-limited adipose tissue compartment. Note the rapid, exponential decay of TCE concentrations following the hour-long exposure period. This simulation illustrates that the perfusion-limited compartmental model may not be able to predict the expected slow accumulation and release of TCE within the adipose tissue. Furthermore, this model may lead to an over-prediction of TCE blood concentrations, as well as an under-prediction of the overall clearance rate for TCE.

3 A PBPK model for TCE with a diffusion-limited adipose tissue compartment

A second type of standard PBPK compartmental model is the diffusion-limited compartment. This model is based on the assumption that the blood flow rate to the tissue is much *faster* than the transport of

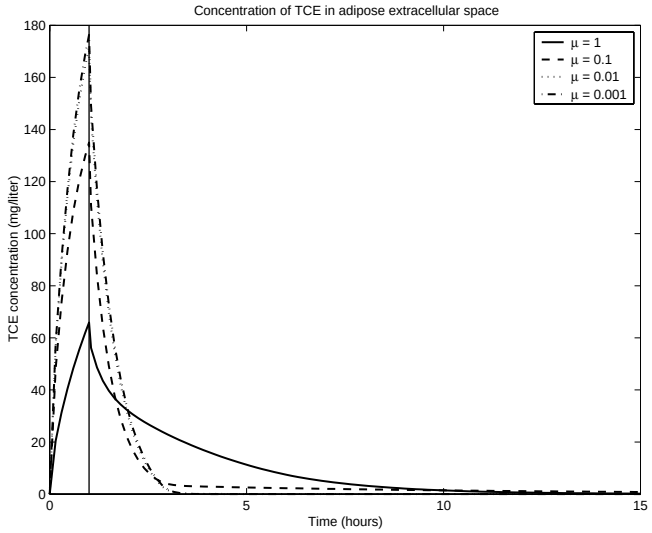

Figure 3: Model simulation: Total concentration of TCE in time in the extracellular subcompartment of the diffusion-limited fat compartment for various values of the permeability coefficient μ.

solute (in this case, TCE) across cell membranes in the tissue [16]. The diffusion-limited compartment is divided into two subcompartments: the intracellular space and the extracellular space, which includes the vascularization and the interstitial fluid. Within each of these subcompartments, rapid equilibrium and uniformity are assumed. The diffusion of solute across the cell membranes is modeled using Fick's first law of diffusion.

In [1, 17] we modified the original PBPK model (1) – (8) for TCE by replacing the perfusion-limited adipose tissue compartment with a diffusion-limited compartment. A new PBPK whole-body model is then formed by coupling the equations (2) – (8) with the following differential equations corresponding to the diffusion-limited adipose tissue compartment:

$$V_{fe}\frac{dC_{fe}}{dt} = Q_f(C_a - \frac{C_{fe}}{P_f}) + \mu(C_{fi} - C_{fe}) \tag{9}$$

$$V_{fi}\frac{dC_{fi}}{dt} = \mu(C_{fe} - C_{fi}), \tag{10}$$

where C_{fe} and C_{fi} denote TCE concentrations in the extracellular and intracellular subcompartments of the adipose tissue, respectively. The parameter μ is the cell membrane permeability coefficient for TCE, and has units liters/hour. See the appendix for a list of parameter values.

Model simulations were computed as before for varying values of the permeability coefficient μ. See Figures 3 and 4 for simulations of intracellular and extracellular adipose TCE concentrations, respectively. Note that the response in the intracellular subcompartment for $\mu = 1$ is similar to the response in the perfusion-limited adipose tissue compartment (Figure 2). Moreover, as μ decreases, the peak concentration of unbound TCE in the intracellular subcompartment also decreases and the post-exposure decay of concentrations is less rapid.

Although this model has greater flexibility than the perfusion-limited model in predicting various concentration profiles, it is important to note that the diffusion-limited model may not be appropriate for TCE in adipose tissue. TCE has a low molecular weight and is highly lipophilic, so that it diffuses rapidly across cell membranes. Therefore the diffusion rate of TCE is likely to be much greater than the rate of blood flow to the adipose tissue and hence the diffusion-limited model may not be physically appropriate in this case.

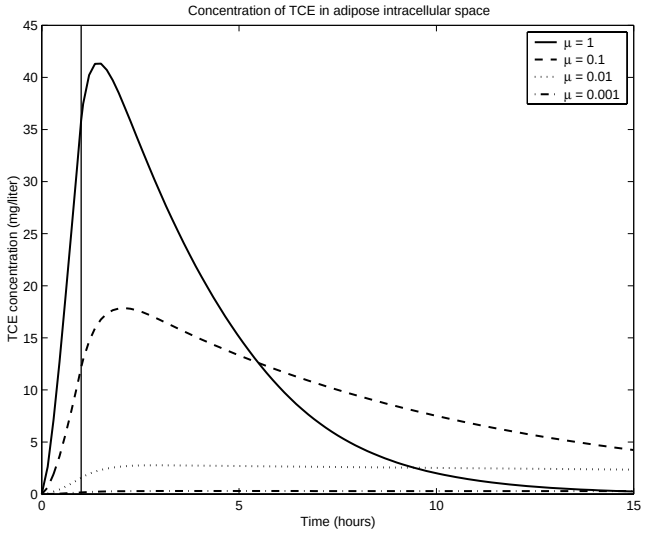

Figure 4: Model simulation: Concentrations of unbound TCE in time in the intracellular subcompartment of the diffusion-limited fat compartment for various values of the permeability coefficient μ.

4 A PBPK-hybrid model for TCE with an axial dispersion-based adipose tissue compartment

In this section we present a PBPK-hybrid model for TCE with a spatially varying compartment for the adipose tissue. As detailed in [1, 17], we have developed an axial dispersion-type model for the transport of TCE inside the adipose tissue, which is designed to account for the physiological heterogeneities seen in the fat. This compartmental model is then coupled with the remaining tissue compartments to create a whole-body PBPK-hybrid model. The dispersion-based compartmental model for the adipose tissue is based on the model of Roberts and Rowland [18] for disposition in the liver, and is adapted for the specific physiology of fat tissue.

A key feature of the dispersion model is that it utilizes a single representative "cell" to capture the transport behavior in a large collection of similar "cells" which have varying properties. The variability among cells is modeled with an axial dispersion term, which has a coefficient known as the axial dispersion number. The axial dispersion number is a model parameter that measures the variability that occurs across the population of cells. See [17, 18] for a detailed discussion of the dispersion model.

In the case of adipose tissue, we choose the representative "cell" to be an adipocyte (fat cell) together with a neighboring capillary, which are both surrounded by the interstitial fluid. This "cell" represents a functional unit within the adipose tissue, as it is well known that each adipocyte is in contact with one or more capillaries [24]. See Figure 5 for an illustration of an adipocyte–capillary unit.

4.1 Model geometry and assumptions

The geometry for the axial dispersion model is based on the structure of the adipocyte–capillary unit. We divide the adipose compartment into three subcompartments which represent the adipocyte, capillary and interstitial space. The adipocyte region (A) is represented by a sphere, and is adjacent to the capillary or blood region (B) that is represented as a circular cylinder which curves around the surface of the adipocyte (see Figure 6). Each of these two regions is surrounded by the interstitial region (I). Although not indicated by the geometry, we assume that the capillary and adipocyte are in direct contact at areas of membrane continuity between the capillary endothelium and the adipocyte plasma membrane. Several studies have indicated the existence of these "interfacial continua" [3, 4, 5, 22], and we include them in the model as an important route of TCE transport within the adipose tissue (see [17]).

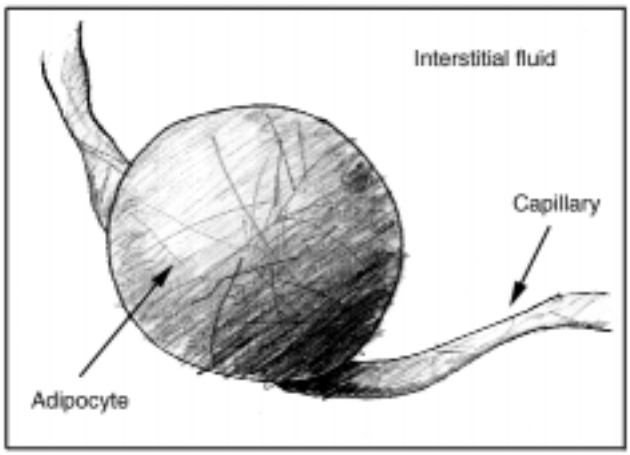

Figure 5: Representation of an adipocyte and capillary, surrounded by interstitial fluid.

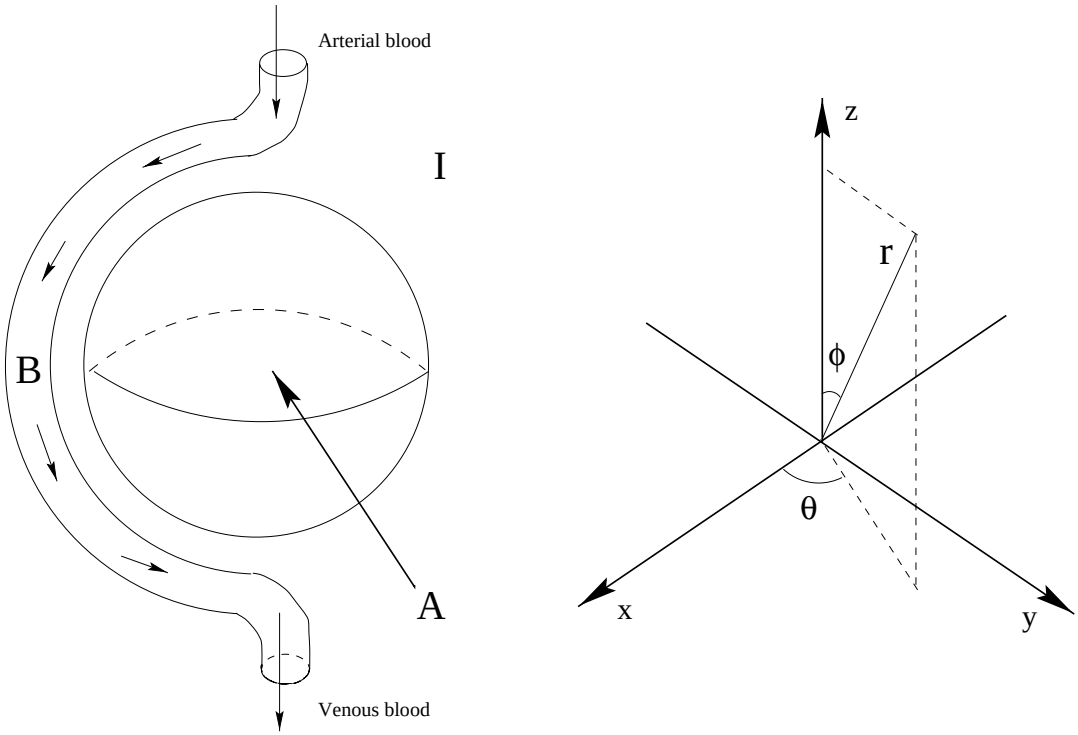

Figure 6: Adipose tissue represented geometrically: the adipocyte region (A) is a sphere, surrounded by the interstitial space (I). The capillary or blood region (B) is a cylindrical tube that wraps around the capillary. Coordinates are in spherical coordinates (r, θ, ϕ).

We assume that blood and TCE flow from the arterial blood compartment into the capillary region of the adipose compartment. As it flows through the capillary, TCE diffuses across the capillary endothelium into and out of the interstitial fluid, as well as into and out of the adipocyte at areas of membrane continuity. At the exit to the capillary, TCE and blood flow from the adipose compartment into the venous blood compartment.

TCE enters and exits the interstitial fluid via the capillary at the location $\theta = \theta_0$, $\varepsilon_1 < \phi < \varepsilon_2$, and from the adipocyte at all points $0 \le \theta \le 2\pi$, $0 \le \phi \le \pi$. The nonuniform interface between the capillary and interstitial space (with respect to θ) results in diffusion of TCE through the interstitial fluid. Similar conditions occur in the adipocyte region.

In the capillary region our set of assumptions results in a partial differential equation that depends only on time and on the spatial variable ϕ. In the other two subcompartments, our assumptions lead to PDEs that depend on time and on the spatial variables θ and ϕ. See [1, 17] for detailed descriptions and justifications of our model geometry and assumptions.

4.2 Model equations

The resulting model equations for the capillary, interstitial fluid and adipocyte subcompartments are given by

$$\begin{aligned}
V_B\frac{\partial C_B}{\partial t} &= \frac{V_B}{r_2\sin\phi}\frac{\partial}{\partial\phi}\left[\sin\phi\left(\frac{\mathcal{D}_B}{r_2}\frac{\partial C_B}{\partial\phi} - vC_B\right)\right] \\
&+ \lambda_I\mu_{BI}(f_I C_I(\theta_0) - f_B C_B) \\
&+ \lambda_A\mu_{BA}(f_A C_A(\theta_0) - f_B C_B) \qquad (11)\\
-\frac{\mathcal{D}_B}{r_2}\frac{\partial C_B}{\partial\phi}(t,\phi) + vC_B(t,\phi)\Big|_{\phi=\varepsilon_1} &= \frac{Q_c}{1000A_B}C_a(t) \qquad (12)\\
-\frac{\mathcal{D}_B}{r_2}\frac{\partial C_B}{\partial\phi}(t,\phi) + vC_B(t,\phi)\Big|_{\phi=\pi-\varepsilon_2} &= \frac{Q_c}{1000A_B}C_v(t) \qquad (13)
\end{aligned}$$

$$\begin{aligned}
V_I\frac{\partial C_I}{\partial t} &= \frac{V_I D_I}{r_1^2}\left[\frac{1}{\sin^2\phi}\frac{\partial^2 C_I}{\partial\theta^2} + \frac{1}{\sin\phi}\frac{\partial}{\partial\phi}\left(\sin\phi\frac{\partial C_I}{\partial\phi}\right)\right] \\
&+ \delta_{\theta_0}(\theta)\chi_B(\phi)\lambda_I\mu_{BI}(f_B C_B - f_I C_I) \\
&+ \mu_{IA}(f_A C_A - f_I C_I) \qquad (14)\\
C_I(t,\theta,\phi) &= C_I(t,\theta+2\pi,\phi) \qquad (15)\\
\frac{\partial C_I}{\partial\theta}(t,\theta,\phi) &= \frac{\partial C_I}{\partial\theta}(t,\theta+2\pi,\phi) \qquad (16)\\
C_I(t,\theta,0) &< \infty \qquad (17)\\
C_I(t,\theta,\pi) &< \infty \qquad (18)
\end{aligned}$$

$$\begin{aligned}
V_A\frac{\partial C_A}{\partial t} &= \frac{V_A D_A}{r_0^2}\left[\frac{1}{\sin^2\phi}\frac{\partial^2 C_A}{\partial\theta^2} + \frac{1}{\sin\phi}\frac{\partial}{\partial\phi}\left(\sin\phi\frac{\partial C_A}{\partial\phi}\right)\right] \\
&+ \delta_{\theta_0}(\theta)\chi_B(\phi)\lambda_A\mu_{BA}(f_B C_B - f_A C_A) \\
&+ \mu_{IA}(f_I C_I - f_A C_A) \qquad (19)\\
C_A(t,\theta,\phi) &= C_A(t,\theta+2\pi,\phi) \qquad (20)\\
\frac{\partial C_A}{\partial\theta}(t,\theta,\phi) &= \frac{\partial C_A}{\partial\theta}(t,\theta+2\pi,\phi) \qquad (21)\\
C_A(t,\theta,0) &< \infty \qquad (22)\\
C_A(t,\theta,\pi) &< \infty, \qquad (23)
\end{aligned}$$

where C_B, C_I and C_A denote the concentrations of TCE in the capillary, interstitial fluid and adipocyte regions, respectively. The two boundary conditions (12) and (13) for the capillary region are based on flux

balance principles, while the periodic boundary conditions (15), (16) and (20), (21) with respect to θ in the other two regions are based on the geometry of the sphere. The conditions of finiteness (17), (18) and (22), (23) with respect to ϕ in the interstitial and adipocyte regions result from the singularity that occurs at the poles of the sphere. A complete derivation of the adipose dispersion model and an explanation of the model parameters are presented in [1, 17].

We combine the adipose compartmental model equations (11) – (23) with the whole-body model equations (2) – (8) to obtain a PBPK-hybrid model for TCE. Issues of well-posedness for this nonlinear system of partial differential equations have been addressed in [2, 17]. Specifically, we used a variational formulation and Galerkin methods to establish the existence of a unique weak solution for an abstract class of nonlinear parabolic systems that includes the TCE PBPK-hybrid model as a special case. Moreover, we have proved the theoretical convergence of the Galerkin scheme that we utilize in our numerical model simulations that we present in Section 4.3, and we have addressed theoretical issues related to the associated parameter estimation problem (see [2, 17]).

4.3 Numerical methods

In this section we present results related to the numerical approximation of the PBPK-hybrid TCE model. We use a finite element method to discretize the partial differential equations in the model and we implement our algorithm in Matlab. Moreover, we demonstrate the theoretically guaranteed convergence of our numerical approximation scheme.

Our numerical method utilizes a weak or variational formulation for the PBPK-hybrid TCE model, which is obtained by multiplying each differential equation (11), (14), (19), (2) – (8) by a function from an appropriate class of test functions and then integrating with respect to the spatial variable. The resulting weak formulation has the form

$$\langle \dot{y}(t), \psi \rangle_{\mathcal{V}^*,\mathcal{V}} + \sigma(y(t), \psi) + \langle g(y(t)), \psi \rangle = \langle f(t), \psi \rangle_{\mathcal{V}^*,\mathcal{V}} \tag{24}$$

for all $\psi \in \mathcal{V}$, where

$$y = [C_B,\ C_I,\ C_A,\ C_v,\ C_{br},\ C_k,\ C_l,\ C_m,\ C_t]^{\mathrm{T}},$$

σ is given a sesquilinear form on the space $\mathcal{V} \times \mathcal{V}$, g is a specified nonlinear function and f is the forcing function (for details see [2, 17]. The state space $\mathcal{V}$ is defined by

$$\mathcal{V} = H^1(\bar{\Omega}_B) \times H^1_{per}(\bar{\Omega}_{IA}) \times H^1_{per}(\bar{\Omega}_{IA}) \times \mathbb{R}^6,$$

where

$$H^1_{per}(\bar{\Omega}_{IA}) = \{u = u(\theta, \phi) \in \bar{\Omega}_{IA} : u(\theta, \phi) = u(\theta + 2\pi, \phi)\},$$

and $\langle \cdot, \cdot \rangle_{\mathcal{V}^*,\mathcal{V}}$ is the standard duality product detailed in [25]. The sets $\bar{\Omega}_B$ and $\bar{\Omega}_{IA}$ are the domains for the capillary region and the interstitial and adipocyte regions, respectively, and are given by $\bar{\Omega}_B = (\varepsilon_1, \pi - \varepsilon_2)$ and $\bar{\Omega}_{IA} = [0, 2\pi] \times [0, \pi]$. See [17] for a complete description and a derivation of the weak form (24).

4.3.1 Finite element formulation

The capillary equation is one-dimensional in space, and we choose uniform subintervals of $[\varepsilon_1, \pi - \varepsilon_2]$ for our discretization nodes in that region. Both the interstitial space and adipocyte equations are two-dimensional in space, and for those regions we choose squares for our discretization meshes.

Using squares in the interstitial and adipocyte regions will allow us to match up the grid points in the ϕ variable with the nodal points in the capillary in a simple and systematic way. Moreover, we can take advantage of the one-dimensional matrix structure for the capillary region to build the matrices for the other two regions using tensors. This leads to a computationally simple and fast implementation in Matlab, (The Mathworks Inc., Natick, MA) which is the programming language we use for our computational work.

Recall that our solution spaces are $H^1(\bar{\Omega}_B)$ for the capillary region and $H^1_{per}(\bar{\Omega}_{IA})$ for the interstitial and adipocyte regions. Based on the smoothness of these spaces, we choose piecewise linear splines for our basis functions in both the ϕ and θ variables. That is, in the capillary region we use piecewise linear splines and for the other two regions we use piecewise bilinear functions.

Note that the solutions C_I and C_A for the interstitial and adipocyte regions respectively are 2π-periodic with respect to θ, as required by the boundary conditions (15) and (20). This suggests that Fourier elements may be chosen instead as basis functions in the θ variable. The δ function with respect to θ that appears in the PDEs (14) and (19) for the interstitial and adipocyte regions, however, suggests that piecewise linear splines may be more appropriate than the global Fourier elements. We tested this hypothesis by implementing and comparing piecewise linear splines with sine/cosine functions as basis functions in the θ variable. The solutions generated with the piecewise linear splines were better able to capture the localized behavior of the δ function around $\theta = \theta_0$ than the solutions generated with sine and cosine basis functions. Here we report on our results related to the piecewise linear basis functions.

For any positive integer N and for some discretization $\phi_1, \ldots, \phi_{N+1}$, we define basis functions $B_j^N(\phi)$ by

$$B_j^N(\phi) = \begin{cases} \frac{\phi - \phi_{j-1}}{\phi_j - \phi_{j-1}} & \text{if} \quad \phi_{j-1} \le \phi \le \phi_j \\ \\ \frac{\phi_{j+1} - \phi}{\phi_{j+1} - \phi_j} & \text{if} \quad \phi_j \le \phi \le \phi_{j+1} \\ \\ 0 & \text{otherwise} \end{cases} \tag{25}$$

for $j = 2, \ldots, N$ and

$$B_1^N(\phi) = \begin{cases} \frac{\phi_2 - \phi}{\phi_2 - \phi_1} & \text{if} \quad \phi_1 \le \phi \le \phi_2 \\ \\ 0 & \text{otherwise} \end{cases} \tag{26}$$

$$B_{N+1}^N(\phi) = \begin{cases} \frac{\phi - \phi_N}{\phi_{N+1} - \phi_N} & \text{if} \quad \phi_N \le \phi \le \phi_{N+1} \\ \\ 0 & \text{otherwise.} \end{cases} \tag{27}$$

In each of the three regions of the adipose tissue compartment, we specify N and $\phi_1, \ldots, \phi_{N+1}$ in order to generate a discretization that includes the capillary boundary points ε_1 and $\pi - \varepsilon_2$, and so that the discretization points in each of the three regions are aligned. Specifically, we set $\varepsilon_1 = \varepsilon_2 = \pi/8$ and $N_\phi = 8\kappa$ for some positive integer $\kappa \ge 1$, and we define

$$\begin{aligned} N_B &= N_\phi - 2\kappa \\ N_I &= N_\phi \\ N_A &= N_\phi. \end{aligned}$$

Moreover, we define the discretization in the capillary region by

$$\phi_j^B = \varepsilon_1 + \frac{(\pi - \varepsilon_2 - \varepsilon_1)(j-1)}{N_B} \tag{28}$$

for $j = 1, \ldots, N_B + 1$. Therefore the basis functions in the capillary are given by (25)–(27) where we set $N = N_B$ and $\phi_j = \phi_j^B$ as in (28) for $j = 1, \ldots, N_B + 1$.

In the interstitial and adipocyte regions respectively, we define the discretizations with respect to ϕ by

$$\phi_j^I = \frac{\pi(j-1)}{N_I}, \quad j = 1, \ldots, N_I + 1 \tag{29}$$

$$\phi_j^A = \frac{\pi(j-1)}{N_A}, \quad j = 1, \ldots, N_A + 1. \tag{30}$$

Our basis functions are then given by (25)–(27) with $N = N_I$ and $\phi_j = \phi_j^I$, $j = 1, \ldots, N_I + 1$ as in (29) for the interstitial space, and with $N = N_A$ and $\phi_j = \phi_j^A$, $j = 1, \ldots, N_A + 1$ as in (30) for the adipocyte region. Note that by design we have $\phi_j^B = \phi_{j+\kappa}^I = \phi_{j+\kappa}^A$ for $j = 1, \ldots, N_B + 1$.

In the interstitial and adipocyte regions we also require basis functions with respect to θ. For each positive integer M we define $\theta_j = 2\pi(j-1)/M$ for $j = 1, \ldots, M+1$, and we define the basis functions $\gamma_j^M(\theta)$

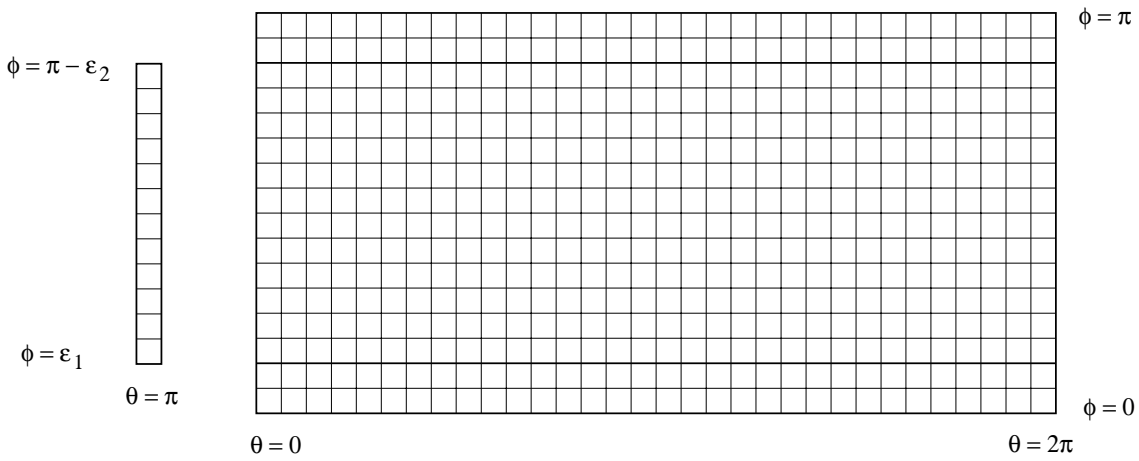

Figure 7: Schematic of an example finite element discretization with $N_\phi = 16$ ($\kappa = 2$). The interstitial and adipocyte regions are each represented by the large rectangle and the capillary region is represented by the smaller rectangle.

to be standard linear splines for $j = 1, \ldots, M+1$. In the interstitial region we set $M = M_I = 2N_\phi$ and in the adipocyte region we set $M = M_A = 2N_\phi$. See Figure 7 for a schematic of the discretizations for each of the three regions with $N_\phi = 16$ ($\kappa = 2$). We denote the total number of variables by N_{tot}, which is given by

$$N_{tot} = (N_B + 1) + (N_I + 1)(M_I + 1) + (N_A + 1)(M_A + 1) + 6.$$

Now let $V_B^N = \text{span}\{B_k^{N_B}\}_{k=1}^{N_B+1}$, and

$$\begin{aligned} V_I^{M,N} &= \text{span}\{\gamma_j^{M_I} B_k^{N_I}\} \\ V_A^{M,N} &= \text{span}\{\gamma_j^{M_A} B_k^{N_A}\} \end{aligned}$$

for $j = 1, \ldots, M_I + 1$, $k = 1, \ldots, N_I + 1$ and for $j = 1, \ldots, M_A + 1$, $k = 1, \ldots, N_A + 1$ respectively. Note that $V_B^N \subset H^1(\bar{\Omega}_B)$, $V_I^{M,N} \subset H^1_{per}(\bar{\Omega}_{IA})$ and $V_A^{M,N} \subset H^1_{per}(\bar{\Omega}_{IA})$. We define the finite-dimensional state space $\mathcal{V}^{M,N}$ by

$$\mathcal{V}^{M,N} = V_B^N \times V_I^{M,N} \times V_A^{M,N} \times \mathbb{R}^6 \subset \mathcal{V}.$$

This space is the subspace of $\mathcal{V}$ that we use for our finite dimensional approximations.

We now define the following approximation functions:

$$C_B^N(t, \phi) = \sum_{n=1}^{N_B+1} u_n(t) B_n^{N_B}(\phi) \tag{31}$$

$$C_I^{M,N}(t, \theta, \phi) = \sum_{n=1}^{N_I+1} \sum_{m=1}^{M_I+1} v_{mn}(t) \gamma_m^{M_I}(\theta) B_n^{N_I}(\phi) \tag{32}$$

$$C_A^{M,N}(t, \theta, \phi) = \sum_{n=1}^{N_A+1} \sum_{m=1}^{M_A+1} w_{mn}(t) \gamma_m^{M_A}(\theta) B_n^{N_A}(\phi). \tag{33}$$

These approximation functions (31) – (33) are then inserted into the weak form (24) with $\psi \in \mathcal{V}^{M,N}$ to obtain the matrix-vector equation

$$\mathcal{M}^{M,N} \dot{y}^{M,N}(t) = \mathcal{A}^{M,N} y^{M,N}(t) + \mathcal{G}(y^{M,N}(t)) + \mathcal{F}(t) \tag{34}$$

$$y^{M,N}(0) = y_0^{M,N}. \tag{35}$$

The matrices $\mathcal{M}^{M,N}$ and $\mathcal{A}^{M,N}$ have dimension $N_{tot} \times N_{tot}$, and the vector-valued functions $\mathcal{G}$ and $\mathcal{F}$ have dimension N_{tot}. A complete description and derivation of the weak form (34) – (35) is presented in [17].

In the interstitial and adipocyte regions, there are singularities in the weak form at the poles $\phi = 0$ and $\phi = \pi$. To remove these singularities, we utilize the finiteness boundary conditions (17), (18) and (22), (23). This results in the elimination of the endpoints $\phi = 0$, $\phi = \pi$ in the conventional way with the requirement that $v_{m,1}(t) \equiv v_{m,(N_I+1)}(t) \equiv 0$. Similarly, we require $w_{m,1}(t) \equiv w_{m,(N_A+1)}(t) \equiv 0$.

4.3.2 Implementation

In this section we outline the procedure used to solve numerically the semi-discrete problem for the PBPK-hybrid model. As discussed in [2, 17], the solutions to our semi-discrete problem theoretically will converge to the solution of the infinite-dimensional model as $M, N \to \infty$.

The integrals in the matrices $\mathcal{M}^{M,N}$ and $\mathcal{A}^{M,N}$ were evaluated analytically, as described in [17]. The form for the forcing function $\mathcal{F}(t)$ was chosen to simulate one hour of exposure to a constant concentration of TCE in the chamber air, followed by $t_f - 1$ hours with zero concentration of TCE, where t_f is the final time of the simulation. That is, we define $C_c(t)$, the chamber air concentration of TCE, by

$$C_c(t) = \begin{cases} 0 & \text{if} \quad t = 0 \\ K & \text{if} \quad 0 < t \leq 1 \\ 0 & \text{if} \quad 1 < t \leq t_f \end{cases} \tag{36}$$

where $K = 200$, 2000 or 4000 parts per million. Note that this leads to a discontinuous forcing function $\mathcal{F} \in L^2(0, t_f)$. In these simulations we set the initial condition y_0 to be identically zero. This simulates an experiment where each of the animals is assumed to have no TCE in its system before being exposed to TCE during the experiment.

The computer code was written and implemented in Matlab, using Versions 6.0.0.88 (Release 12) and 5.3. Computations were conducted on Sun Ultra 5 and Ultra 10 workstations, a Windows ME-based personal computer with a 1.5 GHz Pentium 4 processor, and a Windows 98-based personal computer with a 400 MHz Pentium II processor.

We solved the semi-discrete problem (34), (35) using the Matlab ordinary differential equation solver `ode15s`. This variable order, variable time step solver is designed to solve both stiff and non-stiff systems efficiently, and is based on numerical differentiation formulas [23]. The stiffness of our system of equations (34), (35) varies as a function of the model parameters, which suggests that `ode15s` is an appropriate solver for this model and the associated parameter estimation problems. We set the relative and absolute error tolerances for `ode15s` to 10^{-3}. Moreover, we supplied the solver with the analytic Jacobian, resulting in reduced computational time, especially for parameter sets which led to a stiff system.

4.3.3 Convergence of the numerical scheme

In [2, 17] we established the theoretical convergence of solutions for the system of finite dimensional Galerkin approximations to the solution for our infinite dimensional model system of equations. This convergence can be demonstrated in practice by solving the semi-discrete problem with fixed parameters for increasing values of N and M.

As previously outlined in Section 4.3.1, we set $N = N_\phi = 8\kappa$ and $M = M_I = M_A = 2N_\phi$, where κ is a positive integer. To test the convergence of our numerical scheme, we ran simulations for $t_f = 5$ hours with κ ranging from one to five, resulting in the values $N_\phi = 8, 16, 24, 32, 40$. For values of κ greater than 5 (i.e., $N_\phi > 40$ and $N_{tot} > 6679$), Matlab ran out of memory and was unable to complete the computation.

Figures 8 – 11 illustrate the convergence of the numerical scheme in each of the adipose subcompartments. Concentrations of TCE at the exit to the capillary region and entrance to the venous blood ($\phi = \pi - \varepsilon_2$) are shown in Figure 8. See Figure 9 for unbound TCE concentrations at the point $\theta = \theta_0 = \pi$, $\phi = \pi/2$, which is the point on the "equator" of the interstitial space nearest the interface with capillary. Both of these plots suggest convergence of the approximate solutions, with concentrations at the exit to the capillary appearing to be nearly independent of the grid size.

Figure 10 depicts unbound TCE concentrations at the point $\theta = \theta_0$, $\phi = \pi/2$ in the adipocyte region, and unbound concentrations at the point $\theta = \theta_0$, $\phi = \pi/8 = \varepsilon_1$ in the adipocyte region are given in Figure 11.

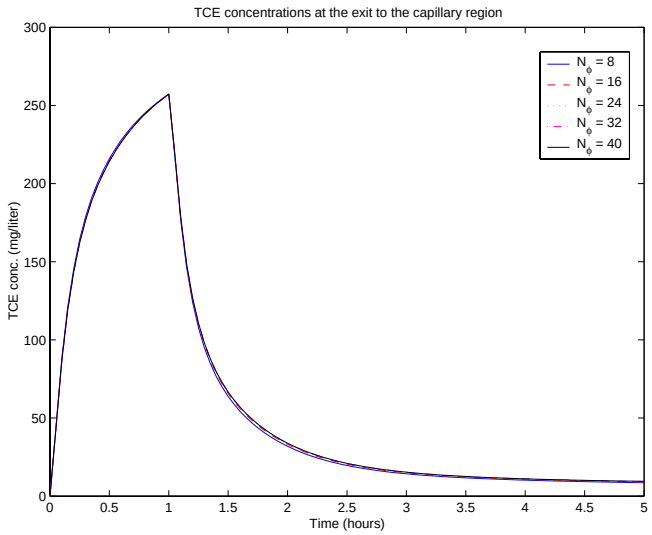

Figure 8: Model simulations at the exit of the capillary region of the adipose tissue for $N = 8, 16, 24, 32, 40$.

Each of these plots also suggests convergence of the numerical scheme, although the solutions appear to differ more significantly for varying values of N than in the other two regions.

As seen in Figure 11, the concentrations in the adipocyte region at $\theta = \theta_0$, $\phi = \varepsilon_1$ appear to be converging most slowly. This point in the adipocyte region is located at the interface with the capillary where the capillary joins with the arterial blood system, and is also located near the pole $\phi = 0$. Recall from Section 4.3.1 that the boundary conditions

$$C_A(t, \theta, 0) < \infty, \qquad C_A(t, \theta, \pi) < \infty$$

require that the coefficients $w_{m,1}(t) \equiv w_{m,M_A+1}(t) \equiv 0$ for all $m = 1, \ldots, N_A + 1$ and $t \geq 0$. This effectively imposes zero boundary conditions at each of the poles in the adipocyte region. Similar boundary conditions apply in the interstitial space.

The continuity of the basis functions dictates that these zero boundary conditions have a major influence on the shape of concentration curves near the poles, especially for small values of N. In general, when $N = 8\kappa$, there are $\kappa - 1$ grid points between the pole $\phi = 0$ and the point $\theta = \theta_0$, $\phi = \varepsilon_1$. Therefore, as κ and N increase, the solutions at the point $\phi = \varepsilon_1$ become less "dependent" on the values at the pole and at the grid points immediately adjacent to the pole. This results in the increasing levels of TCE concentrations at the point $(\theta_0, \varepsilon_1)$ as N becomes large.

4.4 Model simulations

4.4.1 Predicted adipose tissue concentrations

Model simulations were generated for $t_f = 5$ hours with a forcing function chosen to simulate 2000 ppm TCE in the chamber air for one hour, followed by four hours of no exposure. We set $N_\phi = 32$ for our finite element discretization, leading to an overall system of $N_{tot} = 4064$ differential equations. See [17] for a detailed description of model parameters and the appendix for a list of parameter values used for these simulations.

Simulations of capillary TCE concentrations at the points $\phi = \pi/8$, $\pi/4$, $\pi/2$, $3\pi/4$ and $7\pi/8$ are given in Figure 12. These concentration profiles are similar in shape to the concentrations of TCE in the venous blood, shown in Figure 13. In each of these two figures, the concentrations increase sharply during exposure to TCE and then decrease at an exponential rate following exposure. The similarity of behavior in the capillary region and the venous blood compartment is a consequence of the flux boundary condition (13),

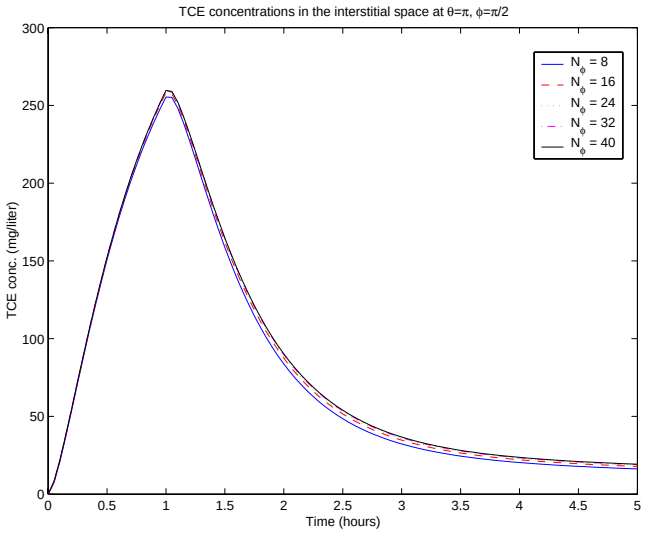

Figure 9: Model simulations in the interstitial region of the adipose tissue for $N = 8, 16, 24, 32, 40$.

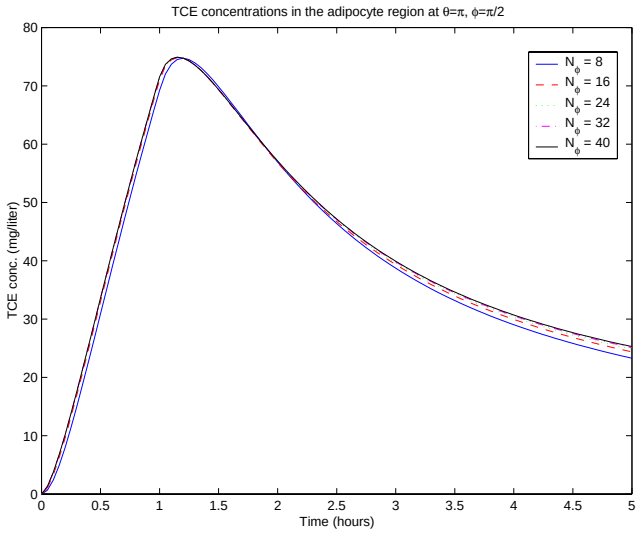

Figure 10: Model simulations in time at the point $\theta = \theta_0 = \pi$, $\phi = \pi/2$ in the adipocyte region of the adipose tissue for $N = 8, 16, 24, 32, 40$.

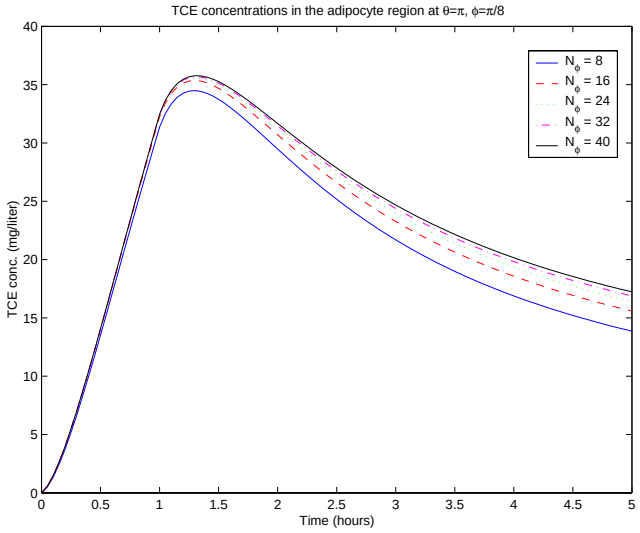

Figure 11: Model simulations in time at the point $\theta = \theta_0 = \pi$, $\phi = \varepsilon_1 = \pi/8$ in the adipocyte region of the adipose tissue for $N = 8, 16, 24, 32, 40$.

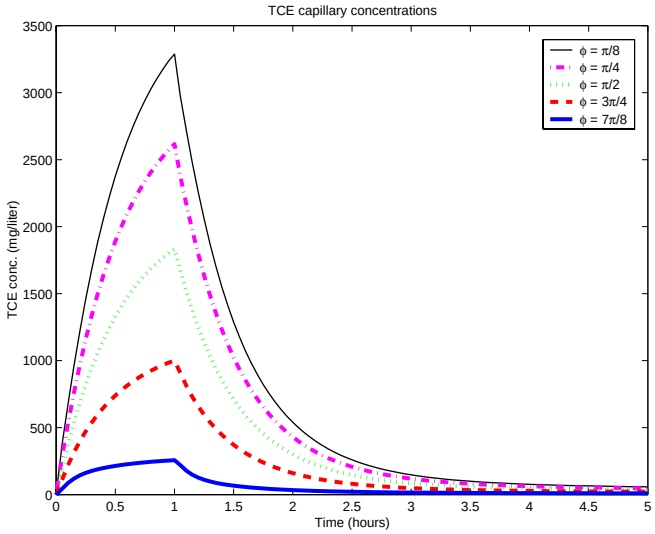

Figure 12: Model simulations: TCE concentrations in time inside the capillary region of the adipose tissue at $\phi = \pi/8$, $\pi/4$, $\pi/2$, $3\pi/4$ and $7\pi/8$.

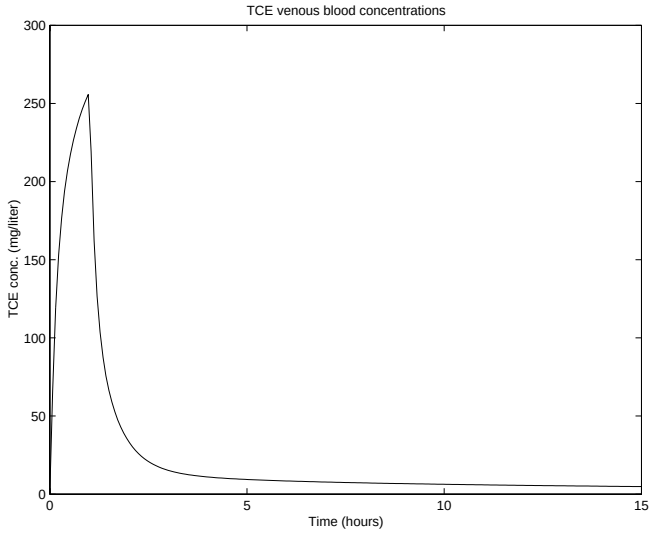

Figure 13: Model simulations: TCE concentrations in time in the venous blood compartment.

and is also consistent with the idea that the dynamics of TCE in the venous blood would be similar (but not necessarily identical) to the dynamics in the capillary.

Figure 14 depicts unbound TCE concentrations in the interstitial region of the adipose tissue at points along the "equator," where $\phi = \pi/2$ and $\theta = 0,\ \pi/4,\ \pi/2,\ 3\pi/4$ and π. These concentrations are similar to those in the venous blood compartment and the capillary region, with less-pronounced peaks. Note that the concentration profile with the largest magnitude is at the point $\theta = \pi = \theta_0$, which is closest in location to the capillary region. Moreover, the concentration profile with the smallest magnitude corresponds to the point $\theta = 0$, which is the furthest point on the "equator" from the capillary region. Note the delay between the maximal value at the point $\theta = \pi$ and the maximal value at $\theta = 0$, which occurs because the TCE must diffuse from the region nearest the capillary around to areas in the interstitial space that are further away from the capillary.

Time snapshots of TCE concentrations on the spherical domain of the interstitial space with $t_f = 3$ can be seen in Figures $15 - 16$. Each individual plot has a color scheme that is *scaled* between the minimum and maximum values *for that point in time*, with red representing the highest concentrations and blue representing the lowest concentrations at that time. The colorbar to the right of each plot indicates the concentration levels that correspond to the color scheme.

The location in the interstitial space nearest the capillary ($\theta = \theta_0 = \pi$) can be seen clearly as the area with the highest concentrations. As time progresses past the hour of TCE exposure, the diffusion term in the model becomes more predominant and the concentrations begin to level out with respect to ϕ and θ, although the highest concentrations remain near the capillary interface.

Figures $17 - 18$ depict time snapshots of concentrations in the adipocyte region. Note that the dynamics are similar to those seen in Figures $15 - 16$ for the interstitial space, although the diffusion term seems to be less dominant in the adipocyte region compared to the interstitial space. This is likely an effect of the differing values of the partition coefficients for each of these two regions, which were estimated using parameter values from [11]. Specifically, the partition coefficient in the adipocyte region is larger than the partition coefficient in interstitial region since TCE is highly soluble in lipids.

See Figure 19 for a simulation in time of TCE concentrations inside the adipocyte region at the points $\phi = \pi/2$ and $\theta = 0,\ \pi/4,\ \pi/2,\ 3\pi/4$ and π. The rate of decay of concentrations in the adipocyte region is slower than the decay rate in the other two adipose regions, which is also a reflection of the higher partition coefficient in the adipocyte region. Note that these concentration profiles look similar to those for the diffusion-limited model in Figure 3.

An important difference between the diffusion-limited model simulations and the dispersion model simulations is that all of the concentration profiles in Figure 19 were generated with fixed permeability coefficients

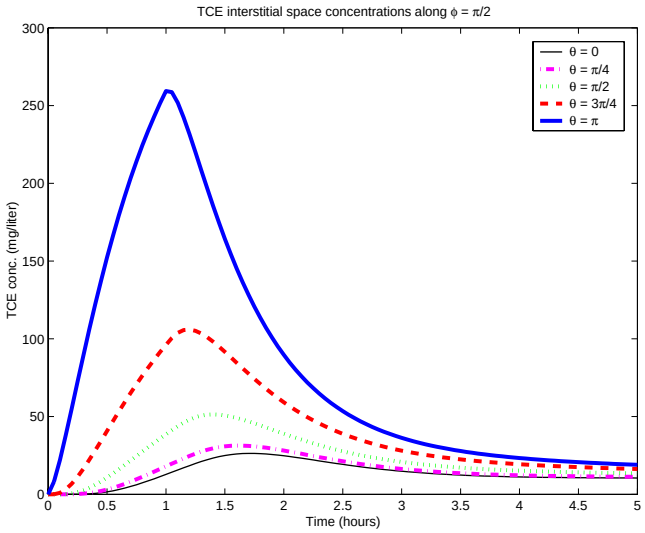

Figure 14: Model simulations: Unbound TCE concentrations in time in the interstitial region of the adipose tissue at the points $\phi = \pi/2$ and $\theta = 0$, $\pi/4$, $\pi/2$, $3\pi/4$ and π.

μ_{BA}, μ_{BI} and μ_{IA} for each of the three regions and with observations taken at various locations, while those shown in Figure 3 were generated with varying values of the permeability coefficient μ. By design, the dispersion model accounts for spatial variation in concentrations within each region of the adipose tissue, and can be used to predict various concentration profiles within the fat.

A simulation for the mean concentration of TCE in the adipocyte region is given in Figure 20. The mean concentration was calculated by taking the average unbound concentration over the discretization points for the finite element approximations:

$$\mathcal{E}[C_A^{M_I,N_\phi}(t_i,\cdot,\cdot)] = \frac{1}{(N_\phi+1)(M_I+1)} \sum_{j=1}^{M_I+1} \sum_{k=1}^{N_\phi+1} f_A C_A^{M_I,N_\phi}(t_i,\theta_j,\phi_k) \tag{37}$$

where in this case we have $N_\phi = 32$ and $M_I = 64$, and θ_j, ϕ_k are given by

$$\begin{aligned} \theta_j &= \frac{2\pi}{M_I}(j-1), \qquad j = 1,\ldots,M_I+1 \\ \phi_k &= \frac{\pi}{N_\phi}(k-1), \qquad k = 1,\ldots,N_\phi+1. \end{aligned}$$

This type of simulation is useful in comparing model predictions with experimental data that are collected from homogenized tissue samples. The data gathered by Evans et al. [11], for example, include unbound TCE concentrations in homogenized samples of liver, brain and fat tissues. Calculating the mean TCE concentration in the adipocyte region allows a comparison of the dispersion model predictions with these experimental data. We have made extensive use of this type of simulation in a study of several parameter estimation problems for our model with simulated data (see [17]).

Note that the predicted concentration profile in Figure 20 is similar to the expected behavior of TCE in adipose tissue (based on experimental data provided to us by M. Evans), with a slow rate of decay following the exposure period. Indeed, the predicted mean TCE adipocyte concentration appears to be more closely matched to this expected transport behavior than the prediction generated by the perfusion-limited adipose tissue compartment. Although the diffusion-limited model yields concentrations similar to those seen for the dispersion model, the diffusion-limited model is based on rate-limiting assumptions that seem incompatible with the transport of TCE in the adipose tissue. As discussed in Section 3, TCE is easy transported across biological membranes, which suggests that the diffusion-limited model may be inappropriate for TCE. The

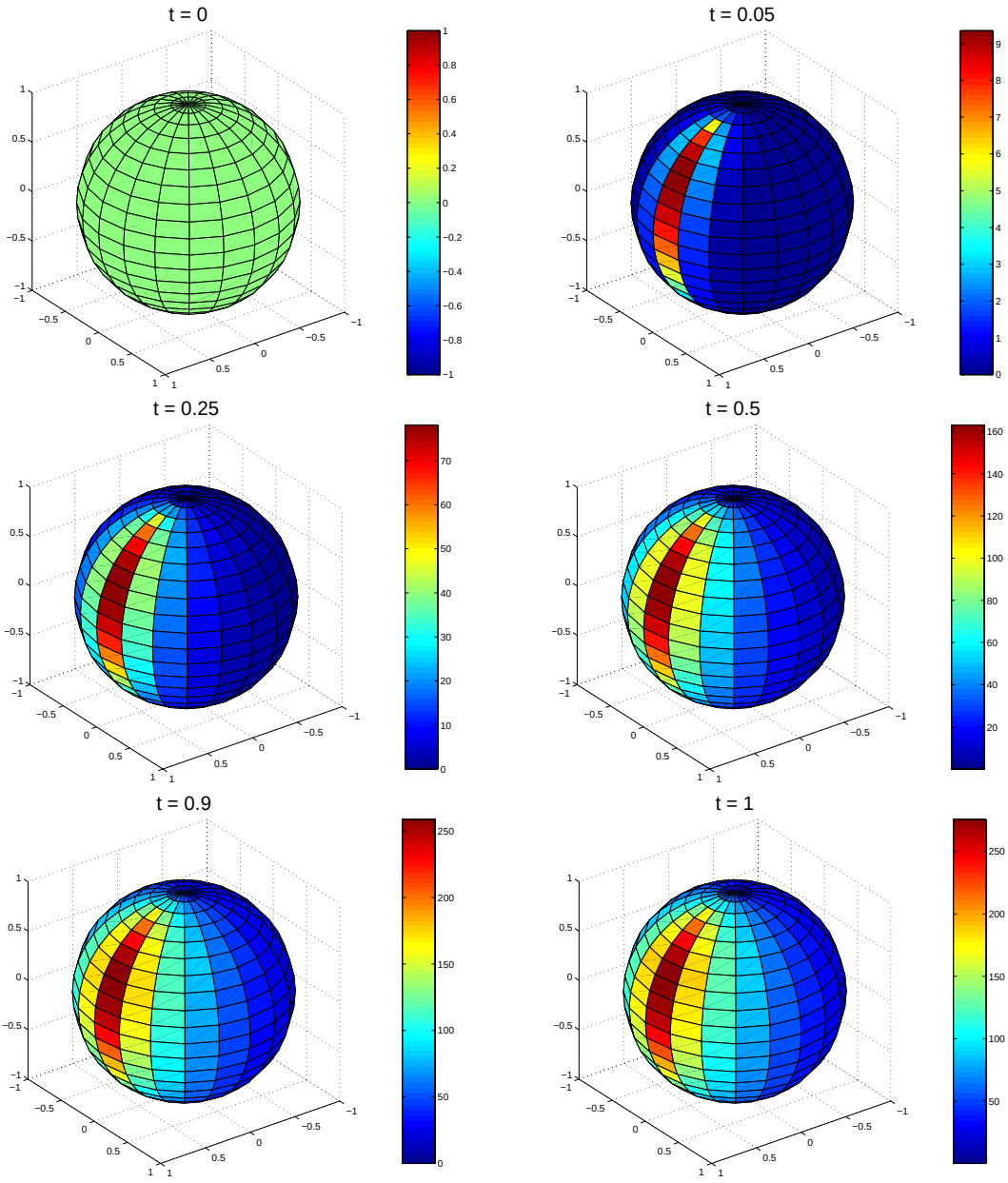

Figure 15: Time snapshots from $t = 0$ to 1 hour of TCE concentrations in the interstitial space.

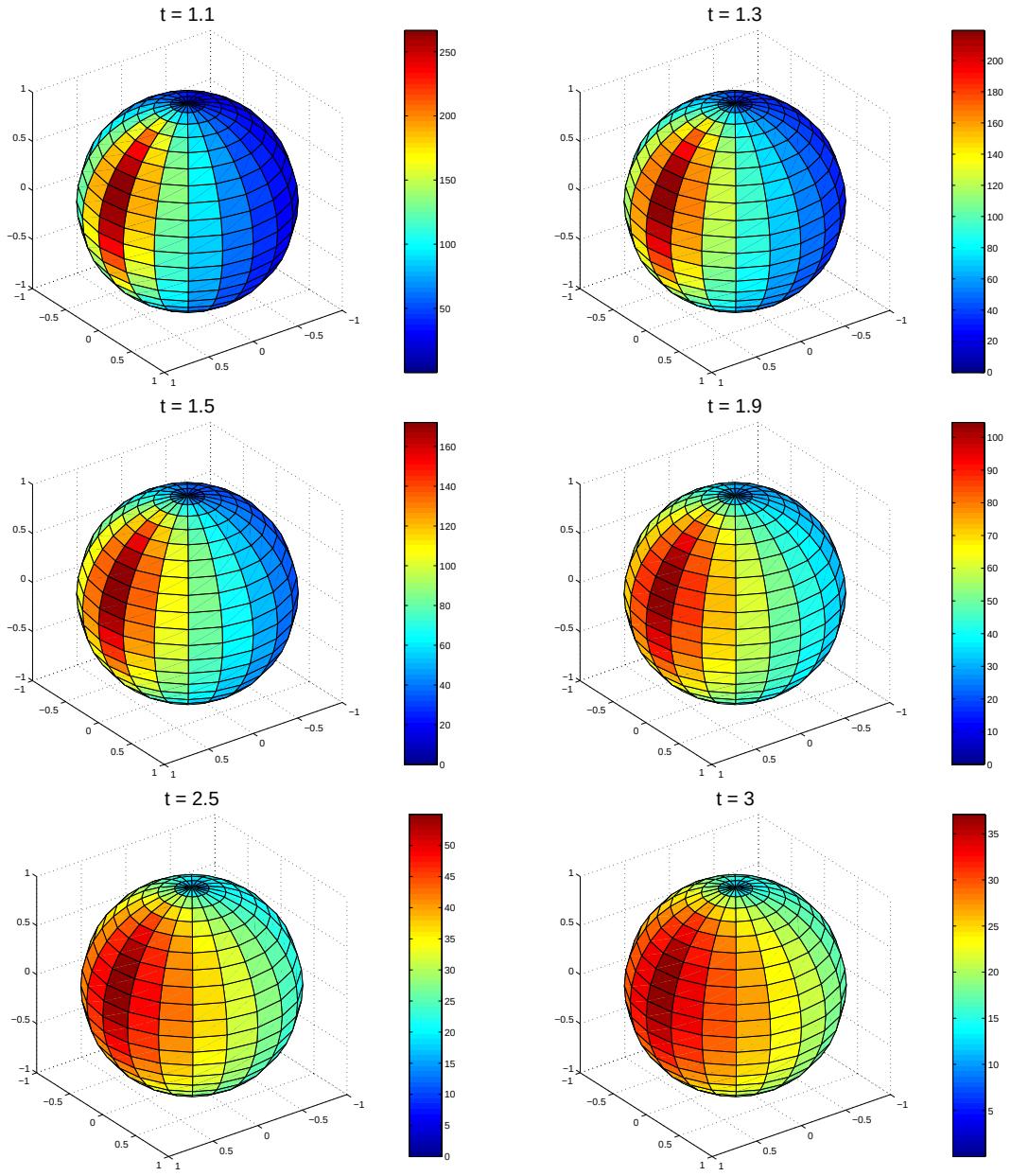

Figure 16: Time snapshots from $t = 1$ to 3 hours of TCE concentrations in the interstitial space.

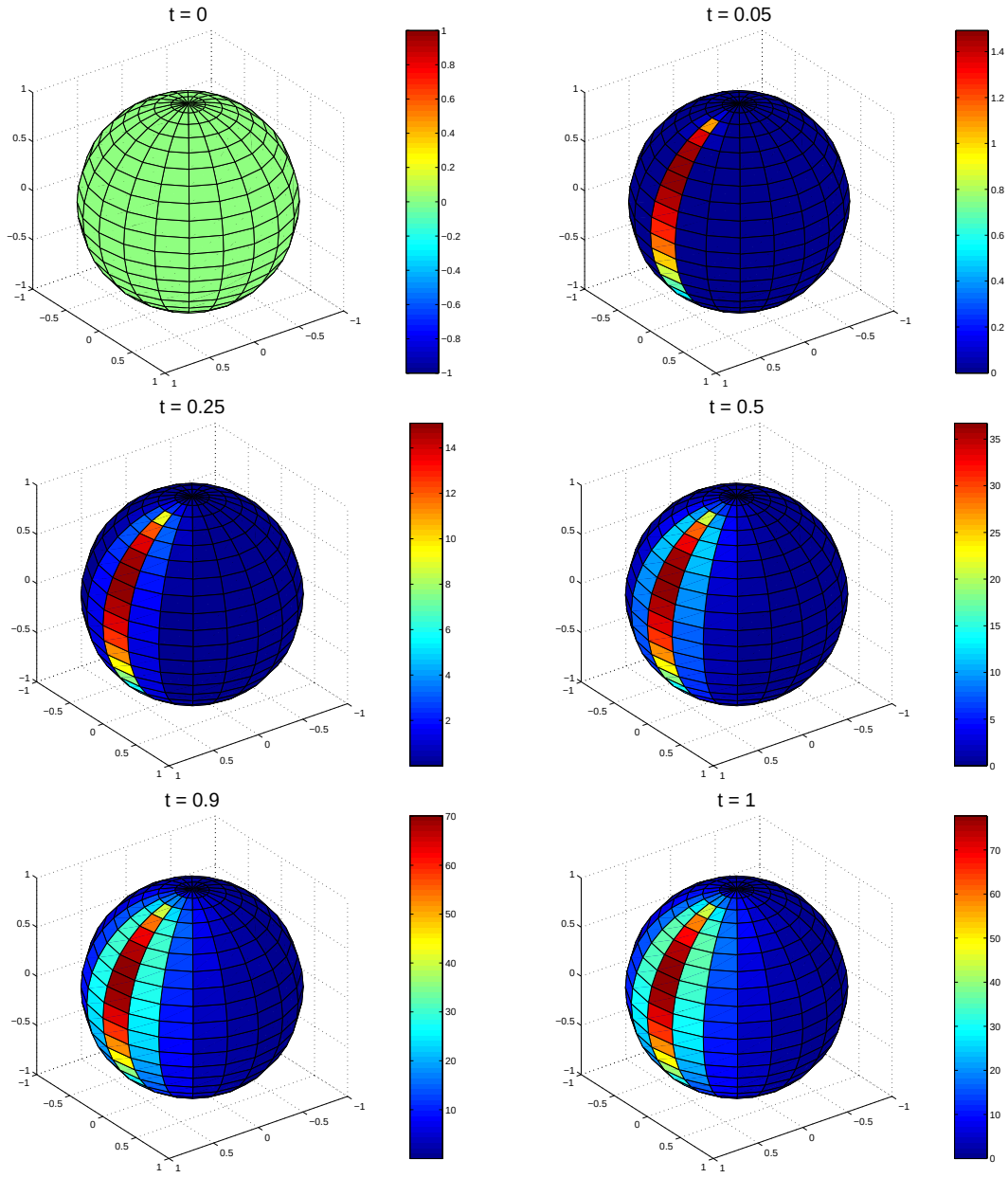

Figure 17: Time snapshots from $t = 0$ to 1 hour of TCE concentrations in the adipocyte region.

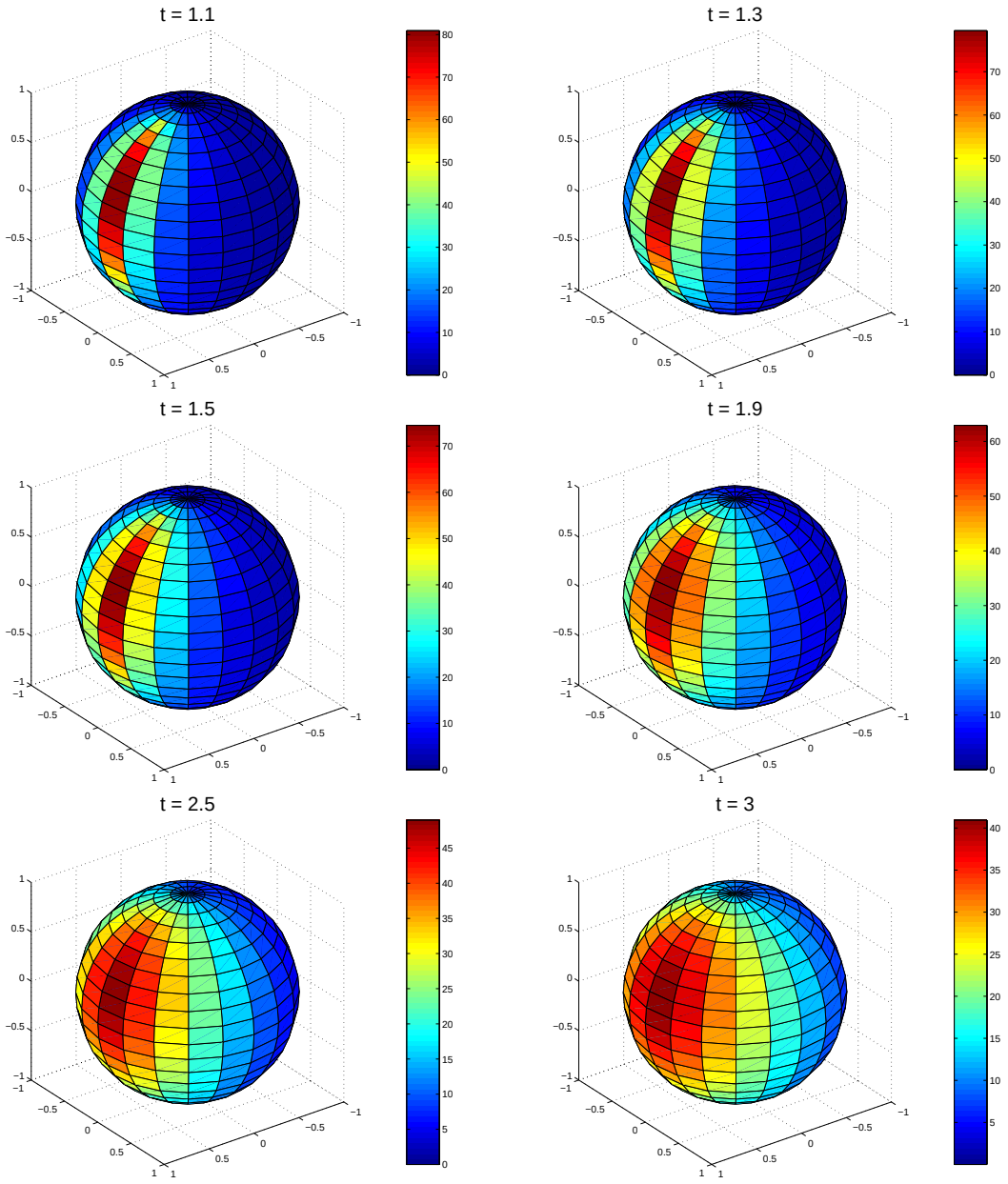

Figure 18: Time snapshots from $t = 1$ to 3 hours of TCE concentrations in the adipocyte region.

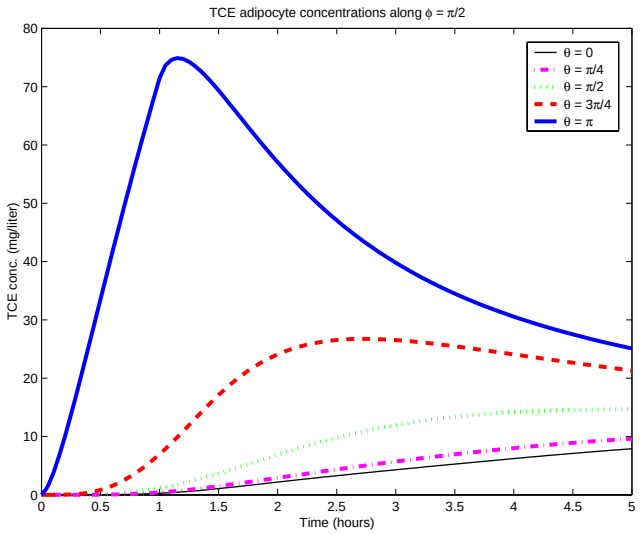

Figure 19: Model simulations: Unbound TCE concentrations in time in the adipocyte region of the adipose tissue at the points $\phi = \pi/2$ and $\theta = 0$, $\pi/4$, $\pi/2$, $3\pi/4$ and π.

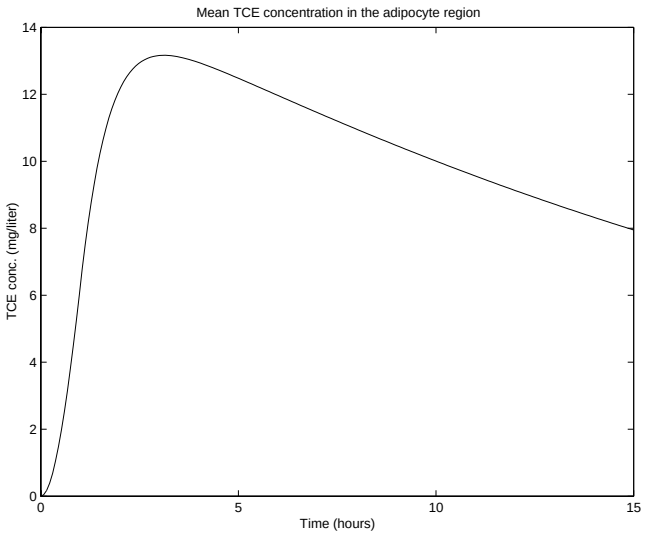

Figure 20: Model simulations: Mean unbound TCE concentration in time in the adipocyte region of the adipose tissue.

axial dispersion-based compartmental model for TCE is based specifically on the heterogeneous physiology of the adipose tissue, and the simulations presented here suggest that this model may be well-suited to predict the adipose and systemic transport of TCE using parameter estimation techniques and experimental data.

5 Concluding remarks

In this paper we have presented three PBPK models for the systemic transport of TCE, each with a different adipose tissue compartment. The first two models are standard PBPK models which are based on assumptions of uniformity and rapid equilibrium within tissue compartments and subcompartments. The perfusion-limited compartmental model yields a rapidly decaying concentration profile of TCE in the adipose tissue, which is likely not a good approximation of TCE's transport and accumulation in the fat. The diffusion-limited compartmental model, which does allow for slower rates of decay and various concentration curves, is not appropriate for this case since TCE is known to diffuse rapidly across cell membranes.

The third PBPK model for TCE includes an axial dispersion-type model for the fat compartment, and is based specifically on the physiology of the adipose tissue. In particular, this spatially varying model was designed to account for the well-established physiological heterogeneities in fat tissue and the expected transport of TCE based on experimental data. Simulations demonstrate the ability of this model to predict TCE concentration profiles in the adipose tissue that are a reasonable match to the expected transport of TCE there. Moreover, this PBPK-hybrid model appears to be well-suited for predicting actual tissue TCE concentrations using parameter estimation techniques and experimental data.

Acknowledgments

This research was supported in part by the U.S. Air Force Office of Scientific Research under grants AFOSR F49620-98-1-0430, AFOSR F49620-98-1-0180, AFOSR F49620-01-1-0026, and in part by an NSF-GRT fellowship (grant GER-9454175) and a P.E.O. Scholar Award to L.K.P. The authors gratefully acknowledge Dr. Marina Evans of the National Health and Environmental Effects Research Laboratory at the U.S. Environmental Protection Agency for her insight and helpful suggestions regarding the TCE models, and for providing us access to experimental TCE data.

Appendix: Model parameters

Parameters for whole-body PBPK model with a perfusion-limited fat compartment. Source: [11].

Model parameter	**Abbr.**	**Estimated value**
Body weight (kg)	bw	0.437
Tissue volumes (liters)		
Blood	V_v	0.0393
Brain	V_{br}	0.0026
Fat	V_f	0.0336
Kidney	V_k	0.002
Liver	V_l	0.017
Muscle	V_m	0.3277
Remaining tissue	V_t	0.0146
Blood flow rates (liters/hr)		
Cardiac output	Q_c	7.6322
Brain	Q_{br}	0.1755
Fat	Q_f	0.6106
Kidney	Q_k	0.6182

Liver	Q_l	1.1448
Muscle	Q_m	2.4423
Remaining tissue	Q_t	2.6407
Ventilation rate (liters/hr)	Q_p	7.6322
Blood/air partition coefficient	P_b	21.9
Tissue/blood partition coefficients		
Brain	P_{br}	0.7671
Fat	P_f	26.26
Kidney	P_k	1.01
Liver	P_l	1.041
Muscle	P_m	0.541
Remaining tissue	P_t	1.041
Michaelis-Menten constant (mg/liters)	k_M	0.18
Metabolic constant (mg/hour)	v_{max}	2.8997

Parameters for diffusion-limited fat compartment.

Model parameter	**Abbr.**	**Estimated value**
Volumes (liters)		
Intracellular space	V_{fi}	0.0269
Extracellular space	V_{fe}	0.0067
Permeability coefficient (liters/hr)	μ	0.1
Blood flow rate to fat (liters/hr)	Q_f	0.6106
Blood/fat partition coefficient	P_f	26.26

Parameters for adipose dispersion model.

Model parameter	**Abbr.**	**Estimated value**
Volumes		
Capillary	V_B	0.0084
Interstitial space	V_I	0.0118
Adipocyte	V_A	0.0135
Unbound fraction		
Capillary	f_B	1
Interstitial space	f_I	0.6667
Adipocyte	f_A	0.0381
Permeability coefficients (liters/hr)		
Capillary – Interstitial space	μ_{BI}	0.02
Capillary – Adipocyte	μ_{BA}	0.03
Interstitial space – Adipocyte	μ_{IA}	0.025
Fraction of transport between the capillary and the other two adipose regions		
Capillary – Interstitial space	λ_I	0.6
Capillary – Adipocyte	λ_A	0.4

Dispersivity coefficient for capillary (m^2/hr)	$\mathcal{D}_B$	1
Diffusion coefficients (m^2/hr)		
Interstitial space	D_I	0.01
Adipocyte	D_A	0.001
Cross-sectional area of capillary (m^2)	A_B	5×10^{-5}
Radius of adipocyte (m)	r_1	0.08
Velocity of blood in capillary (m/hr)	v	0.9769
Reverse Fahraeus-Lindquist parameter	$\mathcal{F}$	0.08
Location (in θ) of capillary central axis	θ_0	π
Points of interface (in ϕ) between capillary and blood compartments		
Capillary – Arterial blood	ε_1	$\pi/8$
Capillary – Venous blood	$\pi - \varepsilon_2$	$7\pi/8$

References

[1] R. A. Albanese, H. T. Banks, M. V. Evans, and L. K. Potter. Physiologically based pharmacokinetic models for the transport of trichloroethylene in adipose tissue. *Tech. Rep. CRSC-TR01-03, Center for Research in Scientific Computation, North Carolina State University, January 2001 (www.ncsu.edu/crsc/reports.html); Bulletin of Mathematical Biology*, submitted.

[2] H. T. Banks and L. K. Potter. Well-posedness results for a class of toxicokinetic models. *Tech. Rep. CRSC-TR01-18, Center for Research in Scientific Computation, North Carolina State University, July 2001 (www.ncsu.edu/crsc/reports.html); Discrete and Continuous Dynamical Systems*, submitted.

[3] E. J. Blanchette-Mackie and R. O. Scow. Lipolysis and lamellar structures in white adipose tissue of young rats: Lipid movement in membranes. *Journal of Ultrastructure Research*, 77:295–318, 1981.

[4] E. J. Blanchette-Mackie and R. O. Scow. Membrane continuities within cells and intercellular contacts in white adipose tissue of young rats. *Journal of Ultrastructure Research*, 77:277–294, 1981.

[5] E. J. Blanchette-Mackie and R. O. Scow. Continuity of intracellular channels with extracellular space in adipose tissue and liver: Demonstrated with tannic acid and lanthanum. *The Anatomical Record*, 203:205–219, 1982.

[6] H. Brauch, G. Weirich, M. A. Hornauer, S. Störkel, T. Wöhl, and T. Brüning. Trichloroethylene exposure and specific somatic mutations in patients with renal cell carcinoma. *Journal of the National Cancer Institute*, 91:854–861, 1999.

[7] J. V. Bruckner, B. D. Davis, and J. N. Blancato. Metabolism, toxicity, and carcinogenicity of trichloroethylene. *Critical Reviews in Toxicology*, 20:31–50, 1989.

[8] R. J. Bull. Mode of action of liver tumor induction by trichloroethylene and its metabolites, trichloroacetate and dichloroacetate. *Environmental Health Perspectives*, 108 Suppl. 2:241–260, 2000.

[9] D. Crandall and M. DiGirolamo. Hemodynamic and metabolic correlates in adipose tissue: Pathophysiologic considerations. *FASEB*, 4:141–147, 1990.

[10] D. Crandall, G. J. Hausman, and J. G. Kral. A review of the microcirculation of adipose tissue: anatomic, metabolic, and angiogenic perspectives. *Microcirculation*, 4:211–232, 1997.

[11] M. V. Evans, W. K. Boyes, P. J. Bushnell, J. H. Raymer, and J. E. Simmons. A physiologically based pharmacokinetic model for trichloroethylene (TCE) in Long-Evans rats. Personal communication, 1999.

[12] A. R. Goeptar, J. N. M. Commandeur, B. van Ommen, P. J. van Bladeren, and N. P. E. Vermeulen. Metabolism and kinetics of trichloroethylene in relation to toxicity and carcinogenicity. relevance of the mercapturic acid pathway. *Chemical Research in Toxicology*, 8:3–21, 1995.

[13] T. Green. Pulmonary toxicity and carcinogenicity of trichloroethylene: Species differences and modes of action. *Environmental Health Perspectives*, 108 Suppl. 2:261–264, 2000.

[14] G. J. Hausman. The comparative anatomy of adipose tissue. In *New Perspectives in Adipose Tissue: Structure, Function and Development*. Butterworths, London, 1985.

[15] L. H. Lash, J. C. Parker, and C. S. Scott. Modes of action of trichloroethylene for kidney tumorigenesis. *Environmental Health Perspectives*, 108 Suppl. 2:225–240, 2000.

[16] M. A. Medinsky and C. D. Klaassen. Toxicokinetics. In *Casarett and Doull's Toxicology: The Basic Science of Poisons*. McGraw-Hill, Health Professions Division, New York, 5th edition, 1996.

[17] L. K. Potter. *Physiologically based pharmacokinetic models for the systemic transport of trichloroethylene*. PhD thesis, North Carolina State University, Raleigh, NC, August 2001.

[18] M. S. Roberts and M. Rowland. A dispersion model of hepatic elimination: 1. Formulation of the model and bolus considerations. *Journal of Pharmacokinetics and Biopharmaceutics*, 14:227–260, 1986.

[19] S. Rosell and E. Belfrage. Blood circulation in adipose tissue. *Physiological Reviews*, 59:1078–1104, 1979.

[20] A. M. Saillenfait, I. Langonne, and J. P. Sabate. Developmental toxicity of trichloroethylene, tetrachloroethylene and four of their metabolites in rat whole embryo culture. *Archives of Toxicology*, 70:71–82, 1995.

[21] C. S. Scott and V. J. Cogliano. Trichloroethylene health risks–state of the science. *Environmental Health Perspectives*, 108 Suppl. 2:159–160, 2000.

[22] R. O. Scow, E. J. Blanchette-Mackie, and L. C. Smith. Transport of lipid across capillary endothelium. *Federation Proceedings*, 39:2610–2617, 1980.

[23] L.F. Shampine and M.W. Reichelt. The MATLAB ODE suite. *SIAM Journal on Scientific Computing*, 18:1–22, 1997.

[24] B. G. Slavin. The morphology of adipose tissue. In *New Perspectives in Adipose Tissue: Structure, Function and Development*. Butterworths, London, 1985.

[25] J. Wloka. *Partial Differential Equations*. Cambridge University Press, Cambridge, 1987.